View metadata, citation and similar papers at core.ac.uk

brought to you by CORE

provided by Aaltodoc Publication Archive

Aalto University

Aaltodoc
OPEN ACCESS

This is an electronic reprint of the original article.
This reprint may differ from the original in pagination and typographic detail.

Author(s): Kivisaari, Pyry

Title: Silicon-Integrated III V Light Emitters and Absorbers Using Bipolar Diffusion

Year: 2020

Version: Final published version

Please cite the original version:

Kivisaari, Pyry. 2020. Silicon-Integrated III V Light Emitters and Absorbers Using Bipolar Diffusion. Physical Review Applied, Volume 13, Issue 6. 064035. DOI: 10.1103/physrevapplied.13.064035.

Rights: © 2020 American Physical Society (APS).

All material supplied via Aaltodoc is protected by copyright and other intellectual property rights, and duplication or sale of all or part of any of the repository collections is not permitted, except that material may be duplicated by you for your research use or educational purposes in electronic or print form. You must obtain permission for any other use. Electronic or print copies may not be offered, whether for sale or otherwise to anyone who is not an authorised user.

Silicon-Integrated *III–V* Light Emitters and Absorbers Using Bipolar Diffusion

Pyry Kivisaari[*]
Engineered Nanosystems Group, Aalto University, P.O. Box 13500, Aalto, FI-00076 Finland

(Received 24 February 2020; revised manuscript received 6 May 2020; accepted 1 June 2020; published 15 June 2020)

The ultimate target for silicon photonics is to merge together all electronic and photonic functions on the same CMOS platform. This requires efficient light emitters and absorbers directly integrated on silicon chips, the lack of which presently forms one of the major bottlenecks for further progress. In this work, a possible solution is presented where diffusion-driven charge transport (DDCT), lateral doping of silicon, and *III–V* nanowire growth are combined to create fully integrated near-surface light emitters and absorbers controlled solely by biasing the underlying silicon wafer. According to the three-dimensional full-device simulations carried out in this paper, DDCT enables high efficiencies for both light emission and photodiode operation in technically feasible silicon-integrated free-standing nanowire structures. Moreover, the results indicate that DDCT is especially well suited for the commonly used 1.55 μm wavelength due to the optimal band-gap difference with silicon, which promotes both a high injection efficiency and low voltage losses.

DOI: 10.1103/PhysRevApplied.13.064035

I. INTRODUCTION

Silicon is the dominant material in the modern microelectronics industry, with its supremacy primarily enabled by the field-effect transistor and the related complementary-metal-oxide-semiconductor (CMOS) technology [1]. This position has later spawned the rapidly expanding field of silicon photonics, with the grand aim of seamless integration of all electronic and photonic functions on the same CMOS platform [2]. Most of the basic building blocks toward this goal, such as optical modulators, beam splitters, resonators, and (de)multiplexers, are already widely available but one of the greatest remaining challenges is to integrate a light source on a silicon chip in an efficient and industrially viable way [2,3]. In particular, light sources based on direct heteroepitaxy on silicon would be beneficial for several reasons, including easier integration with existing silicon devices and the possibility of sharing the same electrical contacting.

Instead of direct heteroepitaxy, currently the established way of light generation in silicon photonics is through so-called hybrid-laser integration, i.e., separately fabricating *III–V* (such as InP) lasers and bonding them on the silicon substrate [2]. Substantial research efforts to realize epitaxially integrated light emitters and absorbers on silicon are, nevertheless, under way, either by enhancing light emission in silicon itself or by integrating other more efficient light-emitting materials [4–18]. However, considering the two perhaps most widely studied approaches, light emitters based on silicon or germanium suffer from more or less indirect band gaps, while those based on *III–V* materials are typically extremely difficult to grow on silicon in planar form. These challenges in turn make light emitters based on *III–V* nanowires (NWs) particularly attractive for heteroepitaxial silicon integration.

III–V NWs have been studied for more than two decades and they do not require lattice matching with the substrate to achieve good crystal quality. Therefore, they are widely regarded as one of the most promising alternatives for direct integration on silicon [19]. Moreover, controlled NW growth on silicon is continuously becoming more feasible owing to long-standing research efforts [20–22]. Numerous works report light emission from NW structures on silicon but most of the demonstrations so far are done with optical pumping [23–31]. Electrical injection of NWs would be the necessary next step to enable their full integration with silicon. However, electrical injection remains challenging using the conventional method, where the NWs (1) require p-n junctions and (2) need to be contacted from the top using somewhat complicated methods and materials prone to absorbing part of the emitted light [32,33].

Figure 1 illustrates a potential solution to the problem of electrical injection of NWs on silicon. In the proposed approach, the NWs are electrically injected without top contacts by taking advantage of diffusion-driven charge transport (DDCT) [34–39] and lateral doping of silicon. DDCT has been previously reported in GaAs [36] and GaN [37–39] light emitters, theoretically as well as experimentally. The simulations of this paper are carried out to show that combined with the remarkable diffusion lengths in silicon and existing lateral-doping techniques,

[*]pyry.kivisaari@aalto.fi

 © 2020 American Physical Society

it offers a path toward fully silicon-integrated electrically injected free-standing NW light emitters and absorbers. Two types of structures are studied here: Fig. 1(a) shows the lateral-injection (LI) structure, where the NW is placed on the same side as the doped areas and contacts, enabling CMOS-compatible device fabrication on practically any commonly used silicon-substrate type, e.g., silicon-on-insulator substrates or weakly doped substrates. Figure 1(b) shows the alternative through-film-injection (TFI) structure for thin films or even thicker bulk silicon wafers, which would allow realization of the lateral doping and nanostructure growth or deposition on different sides of the substrate. This could, in particular, enable extension of the wavelength range of large-area silicon detectors.

In this paper, the standard semiconductor charge-transport equations are solved numerically using a 3D simulation model illustrated in Fig. 1(c) to show that DDCT enables negligible voltage losses and practically unity injection efficiencies in the LI and TFI structures of Fig. 1 with technically achievable device dimensions. For light emission, the results indicate a sweet spot for the NW band gap at around 0.73–0.8 eV, with which both the injection efficiency and the voltage efficiency are high. The corresponding wavelength range is roughly 1.55–1.70 μm, including some of the widely used wavelengths in optical communication. The results also show that DDCT enables efficient photodiode operation, with the photocarrier-collection efficiency generally increasing as the NW band gap increases toward 0.8 eV and above. Also, according to the results, both LED and photodiode operation can be made very efficient in TFI structures with a thin silicon wafer and relatively efficient even with a 300-μm-thick wafer, due to the large diffusion lengths in silicon. Finally, population inversion can also be reached in the NWs with small loss currents and voltage losses, suggesting that laser operation could also be feasible in silicon-based structures using DDCT.

II. THEORY AND METHODS

The full-device operation of the structures in Fig. 1 is studied with the drift-diffusion (DD) model, which relates the electrostatic potential ϕ and the quasi-Fermi potentials ϕ_n and ϕ_p to the electron and hole densities n and p (calculated from Fermi-Dirac statistics) and the total net recombination and generation-rate densities R and G as (for background information and physical justification, see, e.g., Ref. [40])

$$\begin{aligned} \nabla\cdot(-\varepsilon\nabla\phi) &= q\,(p-n+N_d-N_a)\,,\\ \nabla\cdot\mathbf{J}_n &= \nabla\cdot(-q\mu_n n\nabla\phi_n) = q(R-G),\\ \nabla\cdot\mathbf{J}_p &= \nabla\cdot\left(-q\mu_p p\nabla\phi_p\right) = q(G-R), \end{aligned} \tag{1}$$

where q is the elementary charge, N_d and N_a are the ionized donor and acceptor densities, $\mathbf{J}_n$ and $\mathbf{J}_p$ are the electron and hole current density vectors, and μ_n and μ_p are the electron and hole mobilities. The DD model accounts for both drift and diffusion currents with self-consistent electrostatic fields and the total net recombination rate density R is expressed as a sum of the radiative and nonradiative processes, all of which are evaluated from the carrier densities as described in our previous works (see, e.g., Ref. [41]). The generation rate G is otherwise zero, but in Sec. III B it is set to a fixed value in the NW to study the carrier-collection efficiencies of the structures, with more details given at the beginning of Sec. III B.

For heterointerfaces, the relative valence-band positions reported by Van de Walle in Ref. [42] are used,

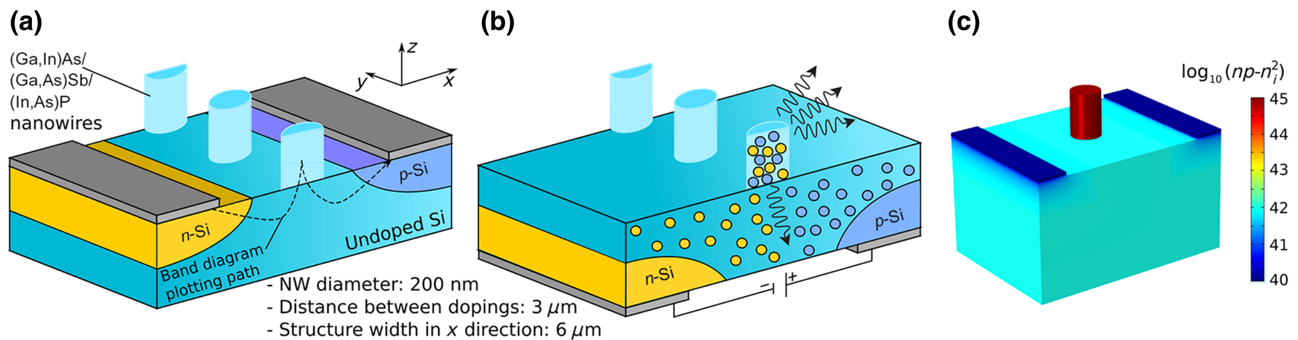

FIG. 1. (a) Lateral-injection (LI) structures applicable for, e.g., silicon-on-insulator substrates or for moderately n- or p-doped substrates. (b) Through-film-injection (TFI) structures to be realized on thin films. (c) A snapshot of the three-dimensional (3D) simulation model of the LI structure with a $Ga_{0.53}InAs$ NW. The color map in (c) shows a base-10 logarithm of the simulated $np-n_i^2$ (n, p, and n_i being the electron density, hole density, and intrinsic carrier density, respectively) at an applied bias of 0.6 V. Position scaling factors are used in the simulation model and therefore the relative distances in (c) do not accurately reflect the true geometry. Also, the color bar in (c) has been cut from its lower end to enable a more informative visualization. Geometrical and other details are given in the beginning of Sec. III. The dashed arrow in (a) shows the plotting path for band diagrams in Appendix B, penetrating roughly 1 μm into the NW.

calculated using the model-solid theory. These are complemented with the experimentally determined band-gap energies and bowing parameters from Ref. [43]. In the present work, carrier transport over heterointerfaces is modeled without separately accounting for possible oxide layers, poorly conducting initial NW growth segments, or interface recombination centers at the silicon-NW interface. While such effects may, depending on their strength, present technical challenges for the efficient operation of these devices, it is also expected that they can be alleviated with careful surface-preparation and growth-optimization steps that are constantly being developed in the field [22]. A more detailed study of interface effects is therefore left out of the present study. Here, the DD model is solved on the 3D domains illustrated in Fig. 1, containing one NW and utilizing symmetries and zero-current boundary conditions at free surfaces. The equation system is solved numerically using an in-house simulation tool that utilizes the finite-element solvers provided by the equation-based user interface of COMSOL MULTIPHYSICS. Corresponding models are widely used to simulate electron-hole dynamics in different kinds of semiconductor light emitters and absorbers [44–47].

Before moving on to the results, the basic operating principle of the devices is shortly qualitatively summarized with the help of Fig. 1(c). When the structures shown in Fig. 1 are used as light emitters, both electrons and holes are injected into the free-standing NW from its bottom side due to the following chain of events. When a forward bias considerably smaller than $E_{g,\mathrm{Si}}/q$ ($E_{g,\mathrm{Si}}$ being the band gap of silicon) is applied, both recombination and leakage in the laterally doped silicon p-i-n junction are weak. Nevertheless, the quasi-Fermi-level separation associated with the applied bias creates a supply of extra electrons and holes all over the intrinsic silicon region owing to carrier diffusion, as illustrated by the quantity $np - n_i^2$ in Fig. 1(c) (n_i being the intrinsic carrier density). Furthermore, the smaller band gap of the NW attracts electrons and holes that are located nearby and consequently also $np - n_i^2$ is orders of magnitude larger in the NW. As nearby-located electrons and holes are thus being injected into the NW, diffusion in silicon simultaneously seeks to maintain homogeneous electron-hole densities everywhere, thereby also spontaneously ensuring a constant supply of electrons and holes next to the NW. Due to the small applied bias, this mechanism and the corresponding recombination rate in the NW can dwarf all other current-generating mechanisms in the device, if the NW lies within the diffusion length from both doped regions. This is confirmed in more detail with the full device simulations to be discussed next.

III. RESULTS AND DISCUSSION

Electroluminescence and photodetection are studied in the structures illustrated in Fig. 1 with the NW band gaps 0.62 eV, 0.73 eV, 0.80 eV, and 0.95 eV, corresponding to different wavelengths of interest for photonic applications: 2.0 μm, 1.70 μm, 1.55 μm, and 1.31 μm, respectively. Results are shown here only for (Ga,In)As NWs [23], but in order to tentatively study whether the trends also hold for differing band offsets and other parameters of the NW, some of the calculations are repeated for (In,As)P [24] and (Ga,As)Sb [48]. The material parameters used in the simulations are listed in Appendix A. In the present simulations, perfectly passivated NW surfaces are assumed, corresponding to zero surface recombination. While surface recombination is generally an important issue in NW devices, the proposed device design is expected to provide surface passivation possibilities that are at least equally good as those of conventional top-contacted NW light emitters and absorbers. In addition, the presence of surface recombination would only add one extra recombination channel for carriers diffusing into the NW. Therefore, here, nonradiative recombination is calculated as a sum of bulk Shockley-Read-Hall (SRH) and Auger recombination and the study of the additional effects of different surface recombination velocities is left for future work.

The distance between the laterally doped regions is 3 μm in the x direction in all the calculations and the circular NW with a diameter of 200 nm is placed in the center of the undoped region (either on the same side or on the other side of the film). The laterally doped regions are 1.5 μm wide in the x direction in the simulation domain, which would correspond to a total width of 3 μm if the structures were repeated in the x direction. The contacts are 500 nm wide, which would similarly correspond to 1-μm-wide contact pads in the repeated structure. The size of the simulation domain in the y direction is chosen such that it would correspond to a distance of 1 μm between the center points of adjacent NWs. The doping pools are 1 μm deep in the z direction in all the structures. Guided by preliminary simulations on how doping densities affect the overall performance, the ionized donor and acceptor densities are set to 10^{19} cm^{-3} to suppress minority carrier leakage but otherwise the doping profiles are unoptimized. The LI structure is 10 μm thick in the z direction and the TFI structures are 1, 10, 100, or 300 μm thick, denoted, respectively, as TFI-1, TFI-10, TFI-100, and TFI-300.

The results are organized as follows. First, in Sec. III A, electroluminescence from 2.5-μm-long uniform NWs is investigated both in the LI and TFI configurations, focusing in particular on the injection efficiency and voltage losses. Section III B focuses on photodiode operation by including a constant generation term in the same NWs and studying the photocarrier-collection efficiency. Then, in Sec. III C, electrical pumping of short NWs is explored to find out whether population inversion can be reached without excessive loss currents or voltage drops to motivate more detailed studies on lasing through DDCT.

A. LED operation with long uniform NWs

Figure 2(a) shows the current-voltage characteristics of the LI structures with 2.5-μm-long (In,Ga)As NWs having different In compositions and therefore different band gaps. The total current is shown per NW, with the idea that these, by themselves, small currents can be multiplied by the number of NWs, if a typical NW array is used instead of a single NW. In Fig. 2(a), the sample with the smallest NW band gap generally exhibits the largest current at low voltages. Moreover, the lower the applied bias, the further apart from each other are the curves of the different samples. This already indicates that bipolar current created by recombination in the NW is the primary current-generating mechanism at low voltages, instead of the competing silicon-diode current. At higher voltages, resistive losses and current over the silicon p-n junction start to dominate the current-voltage behavior, causing the curves in Fig. 2(a) to merge closer to each other.

For additional insight, Fig. 2(b) shows the average quasi-Fermi-level (QFL) separation in the NW as a function of the applied bias. For comparison, Fig. 2(b) also shows the band gaps of the samples (horizontal dotted lines) and the line for which the QFL separation would be equal to the applied bias (dotted line with unity slope). Comparing with Fig. 2(a), the NWs with $E_g = 0.62$–0.80 eV become degenerate at a current of roughly 10 μA, the implications of which are analyzed in more detail in Sec. III C. At small applied biases, on the other hand, all the samples except the one with $E_g = 0.62$ eV ($\lambda = 2.0$ μm) have QFL separations roughly equal to the applied bias, suggesting negligible voltage losses despite the potential barrier between the doped regions and the NW. The worse QFL performance of $E_g = 0.62$ eV as predicted by the simulations correspondingly arises due to the large potential barriers caused by the large band discontinuity between the silicon and the NW. This causes the QFL separation in the NW with $E_g = 0.62$ eV to deviate from the applied bias throughout the whole voltage range shown in Fig. 2(b). More details on this effect are given in Appendix B, with the help of band diagrams.

Focusing more on the potential efficiency of the LI structures as light emitters, Fig. 3(a) shows the injection efficiency (the recombination current in the NW, including radiative and nonradiative recombination, divided by the total current) of the (Ga,In)As LI structures as a function of the current for the different band gaps. Here, all the samples except the one with the largest band gap $E_g = 0.95$ eV ($\lambda = 1.31$ μm) show essentially unity injection efficiencies

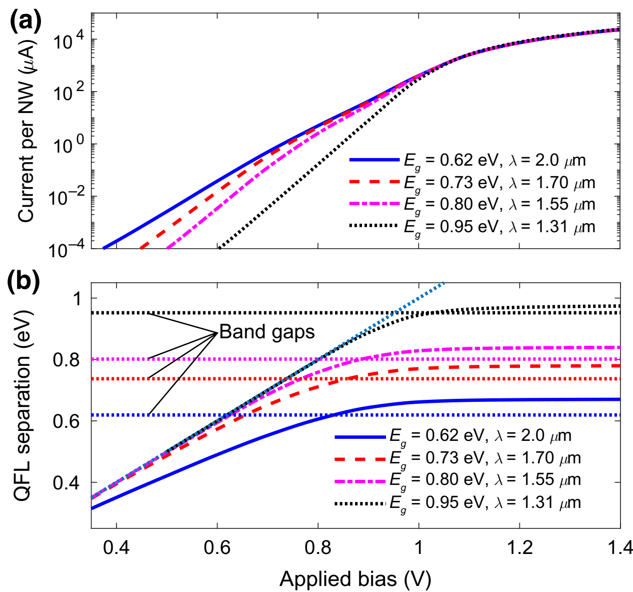

FIG. 2. The (a) current-voltage characteristics and (b) average quasi-Fermi-level (QFL) separation in the NW as a function of the applied bias for the (Ga,In)As LI structures. In (b), the horizontal dotted lines mark the band-gap energies of the different samples and the diagonal dotted line indicates where the QFL separation would be equal to the applied bias, corresponding to zero voltage losses.

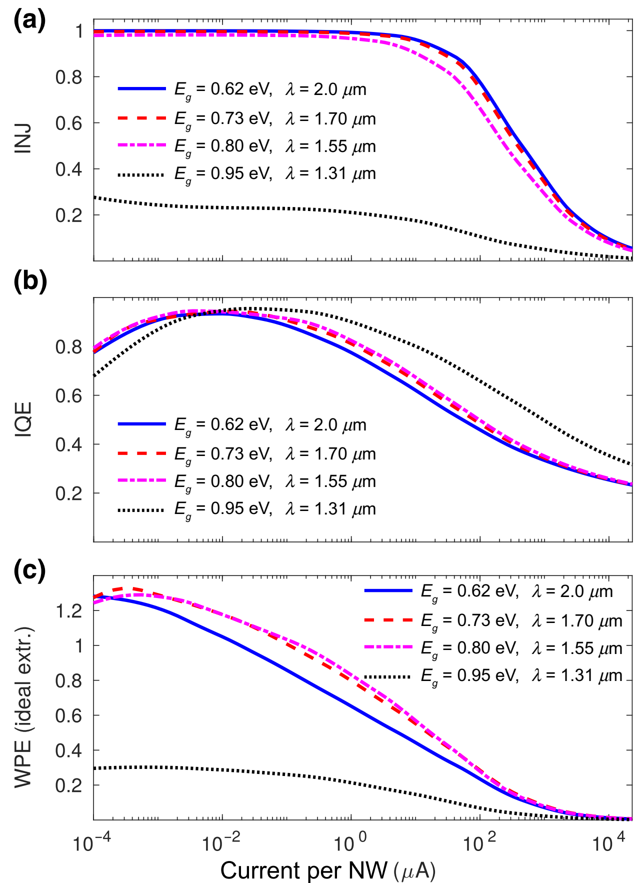

FIG. 3. The (a) injection efficiency, (b) internal quantum efficiency, and (c) wall-plug efficiency (assuming ideal extraction) as a function of the current per NW for the (Ga,In)As LI structures.

up to currents of 10 μA per NW. This indicates that recombination in the low-band-gap NW acts as the dominant charge-carrier sink due to the large electron-hole density, even if both electrons and holes cross paths already in the intrinsic silicon region. However, recombination and leakage of the silicon p-n junction start to decrease the injection efficiency at currents above 10 μA per NW, when the NW becomes degenerate. The sample with the band gap of 0.95 eV has a notably smaller injection efficiency than the other samples already at small currents. Such an abrupt change as compared to the other band gaps is explained by the fact that the NW band gap of 0.95 eV already requires a relatively high voltage for a given NW recombination rate. While the applied biases required for the smaller band gaps entail negligible loss currents in the silicon diode as compared to the NW recombination current, with the band gap of 0.95 eV, the required applied bias results in remarkable loss currents in silicon. This is essentially due to the highly nonlinear dependence of carrier densities on the applied bias. In the case of 0.95 eV, this leads abruptly to an injection efficiency of less than 30%.

To complement the injection efficiency, Fig. 3(b) shows the simulated internal quantum efficiencies (IQE) of the samples, calculated by dividing the net radiative recombination by the total net recombination. The relatively long SRH lifetimes used for the NWs (see Appendix A) result in high IQEs here, but the absolute value of the IQE is not relevant for carrier diffusion to the NWs. One can see that the interplay of radiative and nonradiative processes causes the maximum IQE to lie around 0.01–0.1 μA in all the structures. Finally, the simulated wall-plug efficiencies (WPEs) are shown in Fig. 3(c), calculated assuming ideal extraction as $\eta_{el} = R_{\text{rad}}\hbar\omega/(IV_a)$, where R_{rad} is the net radiative recombination rate integrated over the whole NW, $\hbar\omega$ is the average recombination energy (here assumed equal to E_g for simplicity), I is the total injection current, and V_a is the applied bias. The plotting of the WPE with ideal extraction permits analysis of the attainable performance of the structures without accounting for their optical losses and this provides a useful insight into the general charge-carrier dynamics. In Fig. 3(c), we see, for example, that the attainable WPE does not monotonously follow the NW-band-gap value, this being due to the competing injection and voltage efficiencies: for the sample with $E_g = 0.62$ eV ($\lambda = 2.0$ μm), its QFL losses analyzed in Fig. 2(b) reduce the attainable WPE in spite of the high injection efficiency, while for the sample with $E_g = 0.95$ eV ($\lambda = 1.31$ μm), its poor injection efficiency, shown in Fig. 3(a), is the culprit. Here, the trade-off between voltage losses on the one hand and injection losses on the other means that samples with $E_g = 0.73$ eV (1.70 μm) and particularly $E_g = 0.80$ eV ($\lambda = 1.55$ μm) have the highest WPEs overall. WPE values over unity correspond to the thermophotonic heat-capture effect, where part of the emission energy originates from thermal energy, as explained in more detail in Refs. [49,50].

The results up to now are calculated for LI structures, where the NW is located close to the doped regions and where the presently used dimensions do not provide space for a large number of NWs. Next, to explore the attainable spatial extent of bipolar diffusion and the possibility of increasing the surface area and power of the emitters, the light-emitter operation of the TFI-1, TFI-10, TFI-100, and TFI-300 samples is studied with substrate thicknesses spanning from only 1 μm up to 300 μm. Figure 4 shows the (a) QFL separation in the NW, (b) injection efficiency, and (c) wall-plug efficiency (again assuming ideal extraction) of the (Ga,In)As TFI structures with $E_g = 0.80$ eV (1.55 μm) with the different silicon-substrate thicknesses. In Fig. 4(a), we can see that the TFI-1 and TFI-10 samples

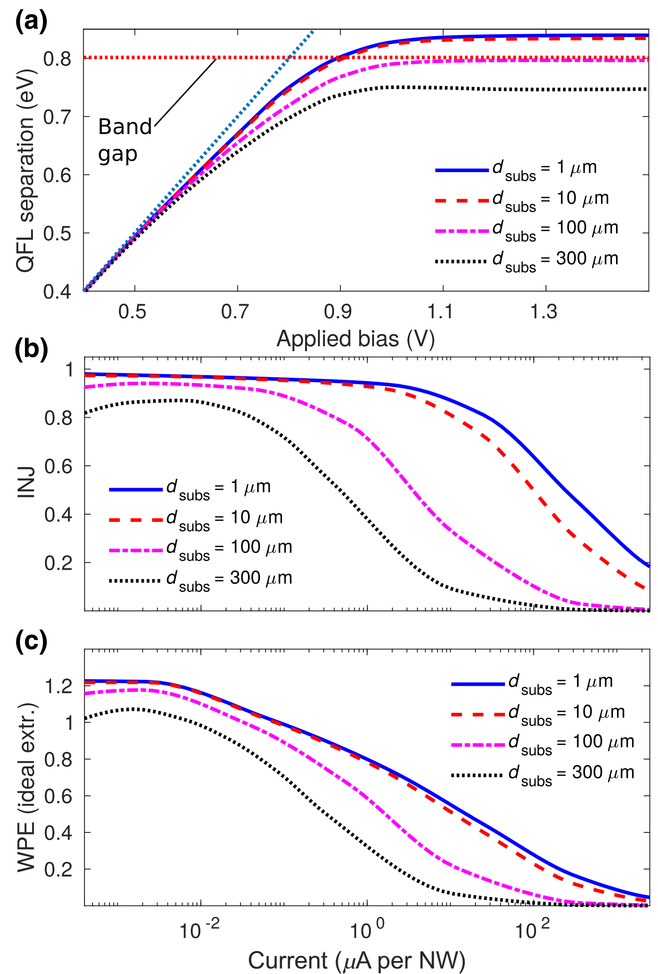

FIG. 4. The (a) average QFL separation in the NW, (b) injection efficiency, and (c) wall-plug efficiency (assuming ideal extraction) of the (Ga,In)As TFI-1, TFI-10, TFI-100, and TFI-300 structures with $E_g = 0.80$ eV. In (a), the horizontal dotted line marks the NW-band-gap energy and the diagonal dotted line indicates where the QFL separation would be equal to the applied bias.

show essentially equally good voltage operation when taken together and even the thick TFI-100 and TFI-300 samples have voltage losses that are almost equally as small as those of TFI-1 and TFI-10 at low applied biases. Interestingly, the TFI-100 and TFI-300 samples do not reach population inversion, as the thick substrates cannot support the corresponding large current densities in the NW.

The injection efficiency of the TFI structures is shown in Fig. 4(b). The TFI-1 and TFI-10 samples show near-unity injection efficiencies, whereas the injection efficiencies are slightly smaller for the TFI-100 and TFI-300 samples, owing to recombination in the substrate, as the substrate is roughly 10^4 times larger in volume than the single NW. One relevant detail here is that, as hinted in Sec. II, current is not allowed to pass through the side walls of the structure and this would correspond to a large periodic structure, with the same structure being repeated in the x and y directions. The combined effects of Figs. 4(a) and 4(b) are again seen in the wall-plug efficiency in Fig. 4(c). There, the difference between the TFI-1 and TFI-10 samples is almost negligible, whereas, overall, the TFI-100 and TFI-300 samples have somewhat smaller WPEs than the thinner samples. All in all, Fig. 4 nonetheless shows that electrons and holes diffuse remarkably well even through the 300-μm-thick silicon substrate, resulting in relatively strong light emission. Note that the TFI structure bears a strong similarity to the design of the highly efficient interdigitated-back-contact (IBC) silicon solar cells [51,52] which, however, are not heterostructure devices.

B. Photodiode operation

In this subsection, the simulations are carried out in the photodiode (PD) mode, where electrons and holes are generated in the NW with the purpose of being collected by the n and p contacts, respectively. To focus on electrical effects, a constant uniform generation rate density is imposed in the NW. Therefore, all the differences to be observed between different samples are only due to their electrical properties and not, for example, due to their potentially different absorption efficiencies. It is well known that NWs can be engineered to be extremely efficient light absorbers [33]. At this stage of the research, determining the carrier-collection efficiencies is therefore interesting in its own right, to provide information solely on the electrical properties of these devices when used as light detectors. The generation rate used in this paper would correspond to a maximum PD current density of 1 nA per NW, should the carrier-collection efficiency be equal to unity. Assuming that the same structure would be used both as the emitter and detector in an optical communication link, this can be compared with currents in the light-emitter case studied in Sec. III A. Note also that the small photocurrent per NW by itself nonetheless corresponds to roughly 3000 mA/cm^2 when divided by the NW cross-section area, i.e., a photocurrent density corresponding to the intensity of well over ten Suns.

Figure 5(a) shows the current-voltage characteristics of the (Ga,In)As LI structures, including all the different band gaps, calculated with the uniform generation rate in the NW. Note that with the generation rate used here, the IQE of the photodiode operation can be obtained by dividing the current by 1 nA per NW. In this paper, this is also referred to as the carrier-collection efficiency. Figure 5(a) shows that with the generation rate chosen here, all the structures with $E_g \geq 0.73$ eV collect more than 70% of the carriers at small negative biases, with only the one with $E_g = 0.62$ eV ($\lambda = 2.0$ μm) showing a clearly worse performance. Additionally, the open-circuit voltages are large (V_{oc} of 0.65 V for $E_g = 0.95$ eV is not visible in the figure) with respect to the NW band gap and therefore they should be measurable in a conventional current-voltage measurement. As all the samples studied in Fig. 5(a) have a similar silicon substrate with equal dopings and mobilities, differences in the PD efficiency as a function of the band gap have to do only with the properties of the NW and its band alignment with silicon. Based on studying the band diagrams (not shown), similar reasons can be identified for the worse performance of $E_g = 0.62$ eV as in the light-emission case, i.e., larger potential barriers next to the NW and smaller carrier densities achieved in silicon to support carrier diffusion.

The somewhat unusual shape of the current-voltage characteristics in Fig. 5(a) is also related to the potential barriers in the structures, which set limits on their

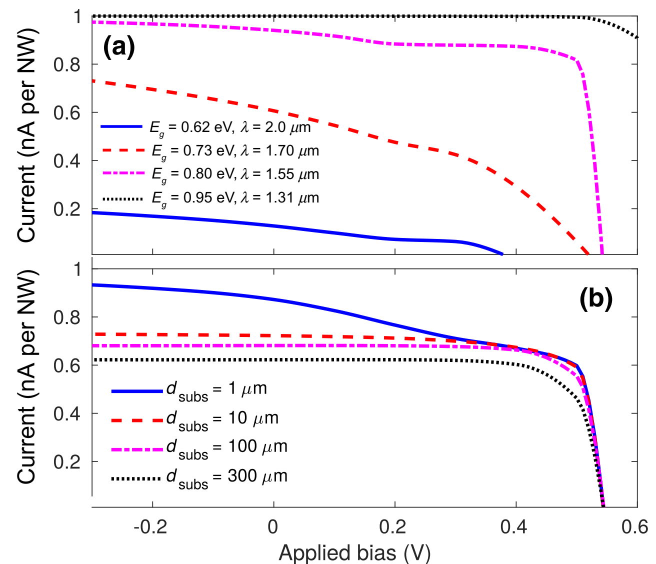

FIG. 5. The current-voltage curves of (a) (Ga,In)As LI structures with different band gaps and (b) (Ga,In)As TFI structures with $E_g = 0.80$ eV under illumination. The uniform generation rate used in the NW corresponds to 1 nA per NW (> 10 Suns) with unity collection efficiency.

carrier-collection efficiency. The fairly large generation rates used here additionally push the limits of bipolar diffusion when it is used to collect all the carriers before they recombine. As a consequence, the increasing bias gradually worsens the balance between (1) desired photocarrier collection over the potential barriers and (2) undesired recombination of photocarriers in the NW, thus causing the unusual shape of the curves. Also, according to further simulations, differences in performance between the different band gaps in Fig. 5(a) increase when the carrier generation rate in the NW increases. In that case, large potential barriers in the samples with small band gaps result in an increasing share of the carriers generated in the NW recombining there instead of diffusing to the contacts. This could be relevant later when calculating the photodiode operation from a full optical simulation, where the spectral intensity of light would determine the eventual carrier generation rate. Calculating the generation rate from an optical simulation would also cause it to have position dependence inside the NW but this is expected to have less influence on the operation owing to efficient carrier spreading inside the NW.

Next, to explore the spatial extension of diffusion in the photodiode mode as well, the carrier collection is studied in the TFI structures with varying substrate thicknesses. Figure 5(b) shows the current-voltage characteristics with generation in the NW for the (Ga,In)As TFI structures with $E_g = 0.80$ eV ($\lambda = 1.55$ μm) with different silicon-substrate thicknesses. In this case, the NW is exactly the same in all the samples and therefore differences between the samples in Fig. 5(b) are only due to differences in the distance that carriers have to diffuse before being collected by the n- and p-type regions. In Fig. 5(b), the TFI-1, TFI-10, TFI-100, and TFI-300 samples all have a short-circuit current of at least 0.6 nA. This corresponds to a carrier-collection efficiency of over 60% even through the thick substrate, and it allows us to substantially extend the detection range of the silicon detectors. Further results calculated for the TFI structures with different band gaps and generation rates (not shown) also reinforce the trend mentioned for the LI structures in the previous paragraph: in general, the larger the NW band gap, the more efficient is the photodiode operation. This resonates well with results for IBC solar cells, which are typically more than 100 μm thick and which reportedly show high photovoltaic efficiencies [51,52]. In silicon IBC cells, the absorbing material is also silicon, which naturally has a larger band gap than 0.80 eV in Fig. 5(b).

C. Population inversion with shorter NWs

If larger emission powers through laser operation are desired, population inversion is needed in the NW in order to make the $(1 - f_c - f_v)$ factor negative and create gain for the appropriate emission wavelengths (f_c and f_v are the electron and hole Fermi-Dirac distribution functions, respectively). In Sec. III A, for example, Fig. 2(b) already shows that the QFL separation in the NW can exceed its band gap, which corresponds to $1 - f_c - f_v$ becoming negative for emission at and slightly above the band-gap energy. However, in the rather long NWs studied in Sec III A, this happens only at rather large current densities per NW due to the relatively large total volume of the uniform NW and the correspondingly large total recombination rate. To explore whether the diffusion-driven structures can be feasible for laser operation with reasonably low expected threshold currents, here the operation of the (Ga,In)As LI structures is studied such that the NW is only 100 nm long. Figure 6 repeats Fig. 2 for short NWs by showing (a) the total current through the single-NW sample and (b) the average QFL separation in the NW as a function of the applied bias for different band gaps of the NW.

Essentially, Fig. 6 shows that population inversion can be reached at modest currents in almost all the cases studied, when stimulated emission is not yet accounted for. The current per NW corresponding to population inversion is marked in the figure for $E_g = 0.80$ eV (approximately 0.8 μA, corresponding to 14 A/cm^2 when normalized with the full sample area), whereas for $E_g = 0.73$ eV and $E_g = 0.62$ eV, it is 0.6 μA and 0.4 μA, respectively. For $E_g = 0.95$ eV, however, the current corresponding to population

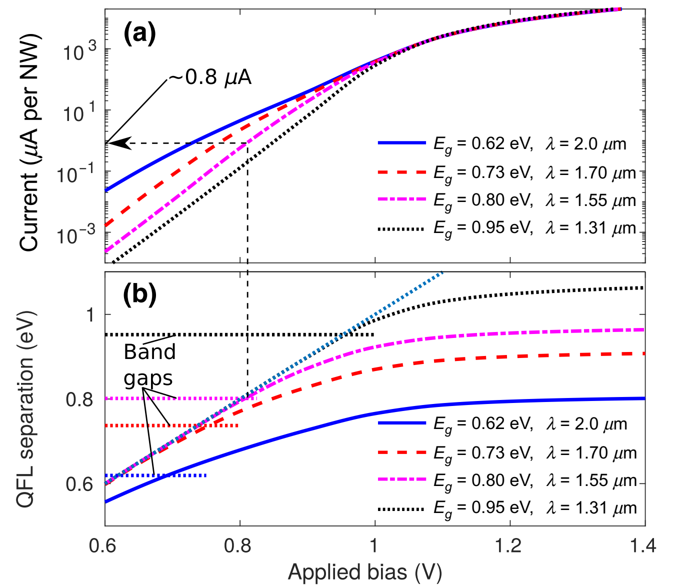

FIG. 6. Figure 2 repeated with short NWs: (a) the current-voltage characteristics and (b) the average QFL separation in the NW in the (Ga,In)As LI structure with the different band gaps, when the NW is only 100 nm long. In (b), the horizontal dotted lines mark the band-gap energies of the different samples and the diagonal dotted line indicates where the QFL separation would be equal to the applied bias.

inversion is roughly 70 μA, due to the higher operating voltage, which also promotes leakage currents and recombination in silicon. To study laser operation, however, the current component owing to stimulated emission would need to be considered separately. Work remains to be done on this topic in the future, so that stimulated emission is also modeled with a laser-cavity structure and an appropriate optical model. However, Fig. 6 provides the first indications that DDCT can even be harnessed to create lasers on silicon, if the structure is engineered for population inversion and stimulated emission. As an alternative for lasing, however, nanoantenna-based light emission for silicon photonics would not require population inversion [53] and the DDCT-based current-injection method studied here could also be attractive for such purposes.

IV. CONCLUSIONS

In this paper, full-device simulations of free-standing *III–V* NWs on laterally doped silicon are carried out to study their feasibility as directly integrated light emitters and absorbers for silicon photonics. According to 3D simulations performed using standard semiconductor-device modeling tools, diffusion-driven charge transport enables such structures to emit light with nearly unity injection efficiency and negligible voltage losses, as well as to operate as efficient photodiodes. The finding of the optimal band gap around the wavelength of 1.55 μm is interesting for optical on-chip communication and it prompts more detailed theoretical and experimental studies on the topic. In particular, future studies should focus on the more detailed design of the device and the choice of the NW material, and to further study the possibility of developing the concept to full optical on-chip communication links.

ACKNOWLEDGMENTS

I gratefully acknowledge the financial support from the Academy of Finland (Grant No. 315403) and the Flagship on Photonics Research and Innovation (PREIN). Computational resources provided by the Aalto Science-IT project were used to carry out the simulations of this paper.

APPENDIX A: PARAMETER VALUES

The parameter values used in the simulations are listed in Table I, based on Refs. [42,43,54]. Note that E_v denotes the topmost valence-band edge in Ref. [42], where spin-orbit splitting is already added. For undoped Si, $\tau_n = \tau_p = 8 \times 10^{-4}$ s is used, corresponding to values reported in Ref. [54] for high-quality silicon with a low background-doping level.

APPENDIX B: BAND DIAGRAMS

To explore the voltage loss related to the smallest NW band gap in Fig. 2(b), Fig. 7 shows the band diagrams of the (In,Ga)As LI structures with (a) the small band gap of 0.62 eV ($\lambda = 2.0$ μm) and (b) the optimal band gap of 0.80 eV ($\lambda = 1.55$ μm). The band diagrams are drawn along the dashed path marked in Fig. 1(a) and the operating points are marked in the figure. In Fig. 7(a), the valence-band QFL E_{Fp} changes much more between silicon and the NW than in Fig. 7(b) due to the overall larger potential barrier for holes in Fig. 7(a). The difference between E_{Fp} and the valence band edge E_V in the bulk silicon region is also marked, with 0.26 eV in Fig. 7(a) and 0.21 eV in Fig. 7(b). The larger energy difference between E_{Fp} and E_V in the bulk silicon region in Fig. 7(a) and the larger potential barrier right next to the NW cause its larger QFL loss. This QFL loss is also responsible for the worse voltage performance observed in Fig. 2(b). Such behavior can generally be expected when the band-gap difference is large between the NW and the laterally doped substrate and supplemental simulations also reproduce it when the NW is (In,As)P with $E_g = 0.62$ eV (not shown).

TABLE I. The material parameters used in the simulations [42,43,54]. Here, E_g is the band gap, λ is the corresponding wavelength in vacuum, E_v and E_c are the valence- and conduction-band-edge energies, ε is the static permittivity, μ_n and μ_p are the electron and hole mobilities, m_e and m_h are the effective masses of the electrons and holes, τ_n and τ_p are the SRH lifetimes of the electrons and holes, B is the radiative recombination coefficient, and C is the Auger recombination coefficient.

Property	E_g	λ	E_v	E_c	ε	μ_n	μ_p	m_e	m_h	τ_n	τ_p	B	C
Si	1.12	1.11	0	1.12	11.70	1400	450	1.084	0.81	0.4 (p-Si)	0.1 (n-Si)	0.00011	0.14
$Ga_{0.35}InAs$	0.62	2.0	0.38	1.00	14.18	28975	465	0.040	0.553	1.07	3.00	3.24	7.00
$Ga_{0.47}InAs$	0.73	1.70	0.35	1.08	13.90	25195	453	0.045	0.571	1.33	3.00	3.97	7.00
$Ga_{0.53}InAs$	0.80	1.55	0.33	1.13	13.77	23305	447	0.048	0.578	1.47	3.00	4.33	7.00
$Ga_{0.66}InAs$	0.95	1.31	0.30	1.25	13.50	19210	434	0.053	0.590	1.75	3.00	5.13	7.00
Units	eV	μm	eV	eV	ε_0	$cm^2/(V s)$	$cm^2/(V s)$	m_0	m_0	s $\times 10^{-7}$	s $\times 10^{-6}$	m^3/s $\times 10^{-16}$	m^6/s $\times 10^{-41}$

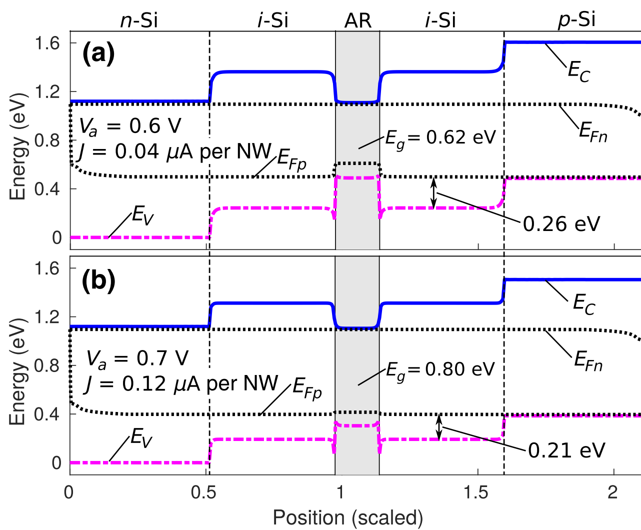

FIG. 7. The band diagrams of the (Ga,In)As LI structures along the dashed path marked in Fig. 1(a) with the NW band gaps of (a) 0.62 eV and (b) 0.80 eV. The operating points are marked in the figure.

[1] D. Liang, M. Fiorentino, and R. G. Beausoleil, in *Silicon Photonics III: Systems and Applications* (Springer, Berlin, 2016), 1st ed.

[2] D. Thomson, A. Zilkie, J. E. Bowers, T. Komljenovic, G. T. Reed, L. Vivien, D. Marris-Morini, E. Cassan, L. Virot, J. M. Fédéli, J. M. Hartmann, J. H. Schmid, D.-X. Xu, F. Boeuf, P. O'Brien, G. Z. Mashanovich, and M. Nedeljkovic, Roadmap on silicon photonics, J. Opt. **18,** 073003 (2016).

[3] S. Chen, Challenges facing silicon photonics technology, *SPIE Photonics West Show Daily*, Feb. 7, (2019), p. 3.

[4] D. Liang and J. E. Bowers, Recent progress in lasers on silicon, Nat. Photon. **4,** 511 (2010).

[5] Z. Fang, Q. Y. Chen, and C. Z. Zhao, A review of recent progress in lasers on silicon, Opt. Laser Technol. **46,** 103 (2013).

[6] B. Corbett, C. Bower, A. Fecioru, M. Mooney, M. Gubbins, and J. Justice, Strategies for integration of lasers on silicon, Semicond. Sci. Technol. **28,** 094001 (2013).

[7] H. Rong, S. Xu, Y.-H. Kuo, V. Sih, O. Cohen, O. Raday, and M. Paniccia, Low-threshold continuous-wave Raman silicon laser, Nat. Photon. **1,** 232 (2007).

[8] M. A. Ferrara, L. Sirleto, G. Nicotra, C. Spinella, and I. Rendina, Enhanced gain coefficient in Raman amplifier based on silicon nanocomposites, Photonics Nanostruct.—Fundamentals Appl. **9,** 1 (2011).

[9] F. Priolo, T. Gregorkievicz, M. Galli, and T. F. Krauss, Silicon nanostructures for photonics and photovoltaics, Nat. Nanotechnol. **9,** 19 (2014).

[10] X. Sun, J. Liu, L. C. Kimerling, and J. Michael, Room-temperature direct bandgap electroluminescence from Ge-on-Si light-emitting diodes, Opt. Lett. **34,** 1198 (2009).

[11] S.-L. Cheng, J. Lu, G. Shambat, H.-Y. Yu, K. Saraswat, J. Vuckovic, and Y. Nishi, Room temperature 1.6 μm electroluminescence from Ge light emitting diode on Si substrate, Opt. Expr. **17,** 10019 (2009).

[12] R. E. Camacho-Aguilera, Y. Cai, N. Patel, J. T. Bessette, M. Romagnoli, L. C. Kimerling, and J. Michel, An electrically pumped germanium laser, Opt. Expr. **20,** 11316 (2012).

[13] S. Liebich, M. Zimprich, A. Beyer, C. Lange, D. J. Franzbach, S. Chatterjee, N. Hossain, S. J. Sweeney, K. Volz, B. Kunert, and W. Stolz, Laser operation of Ga(NAsP) lattice-matched to (001) silicon substrate, Appl. Phys. Lett. **99,** 071109 (2011).

[14] N. Koukourakis, C. Bückers, D. A. Funke, N. C. Gerhardt, S. Liebich, S. Chatterjee, C. Lange, M. Zimprich, K. Volz, W. Stolz, B. Kunert, S. W. Koch, and M. R. Hofmann, High room-temperature optical gain in Ga(NAsP)/Si heterostructures, Appl. Phys. Lett. **100,** 092107 (2012).

[15] O. Jambois, F. Gourbilleau, A. J. Kenyon, J. Montserrat, R. Rizk, and B. Garrido, Towards population inversion of electrically pumped Er ions sensitized by Si nanoclusters, Opt. Expr. **18,** 2230 (2010).

[16] K. S. Ni, H. Krzyzanowska, Y. Fu, and P. M. Fauchet, in *8th IEEE International Conference on Group IV Photonics* (IEEE, London, UK, 14–16 September 2011), p. 202.

[17] A. Lee, Q. Jiang, M. Tang, A. Seeds, and H. Liu, Continuous-wave InAs/GaAs quantum-dot laser diodes monolithically grown on Si substrate with low threshold current densities, Opt. Expr. **20,** 22181 (2012).

[18] A. Y. Liu, S. Srinivasan, J. Norman, A. C. Gossard, and J. E. Bowers, Quantum dot lasers for silicon photonics, Photon. Res. **3,** B1 (2015).

[19] E. Barrigón, M. Heurlin, Z. Bi, B. Monemar, and L. Samuelson, Synthesis and applications of III-N nanowires, Chem. Rev. **119,** 9170 (2019).

[20] T. Mårtensson, C. P. T. Svensson, B. A. Wacaser, M. W. Larsson, W. Seifert, K. Deppert, A. Gustafsson, L. R. Wallenberg, and L. Samuelson, Epitaxial III–V nanowires on silicon, Nano Lett. **4,** 1987 (2004).

[21] K. Tomioka, T. Tanaka, S. Hara, K. Hiruma, and T. Fukui, III–V nanowires on Si substrate: Selective-area growth and device applications, IEEE J. Sel. Top. Quant. **17,** 1112 (2011).

[22] J. Vukajlovic-Plestina, W. Kim, L. Ghisalberti, G. Varnavides, G. Tütüncuoglu, H. Potts, M. Friedl, L. Güniat, W. C. Carter, V. G. Dubrovskii, and A. Fontcuberta i Morral, Fundamental aspects to localize self-catalyzed III–V nanowires on silicon, Nat. Commun. **10,** 869 (2019).

[23] Y. Han, W. K. Ng, C. Ma, Q. Li, S. Zhu, C. C. S. Chan, K. W. Ng, S. Lennon, R. A. Taylor, K. S. Wong, and K. M. Lau, Room-temperature InP/InGaAs nano-ridge lasers grown on Si and emitting at telecom bands, Optica **5,** 918 (2018).

[24] M. Takiguchi, A. Yokoo, K. Nozaki, M. D. Birowosuto, K. Tateno, G. Zhang, E. Kuramochi, A. Shinya, and M. Notomi, Continuous-wave operation and 10-Gb/s direct modulation of InAsP/InP sub-wavelength nanowire laser on silicon photonic crystal, APL Photon. **2,** 046106 (2017).

[25] R. Chen, T.-T. D. Tran, K. W. Ng, W. S. Ko, L. C. Chuang, F. G. Sedgwick, and C. Chang-Hasnain, Nanolasers grown on silicon, Nat. Photon. **5,** 170 (2011).

[26] M. Hocevar, G. Immink, M. Verheijen, M. Akopian, V. Zwiller, L. Kouwenhoven, and E. Bakkers, Growth and optical properties of axial hybrid III–V/silicon nanowires, Nat. Commun. **3**, 1266 (2012).

[27] K. W. Ng, W. S. Ko, T.-T. D. Tran, R. Chen, M. V. Nazarenko, F. Lu, V. G. Dubrovskii, M. Kamp, A. Forchel, and C. J. Chang-Hasnain, Unconventional growth mechanism for monolithic integration of III–V on silicon, ACS Nano **7**, 100 (2013).

[28] H. Kim, W.-J. Lee, A. C. Farrell, J. S. D. Morales, P. Senanayake, S. V. Prikhodko, T. J. Ochalski, and D. L. Huffaker, Monolithic InGaAs nanowire array lasers on silicon-on-insulator operating at room temperature, Nano Lett. **17**, 3465 (2017).

[29] T. Stettner, T. Kostenbader, D. Ruhstorfer, J. Bissinger, H. Riedl, M. Kaniber, G. Koblmüller, and J. J. Finley, Direct coupling of coherent emission from site-selectively grown III–V nanowire lasers into proximal silicon waveguides, ACS Photonics **4**, 2537 (2017).

[30] T. Frost, S. Jahangir, E. Stark, S. Deshpande, A. Hazari, C. Zhao, B. S. Ooi, and P. Bhattacharya, Monolithic electrically injected nanowire array edge-emitting laser on (001) silicon, Nano Lett. **14**, 4535 (2014).

[31] L. C. Chuang, F. G. Sedgwick, R. Chen, W. S. Ko, M. Moewe, K. W. Ng, T.-T. D. Tran, and C. Chang-Hasnain, GaAs-based nanoneedle light emitting diode and avalanche photodiode monolithically integrated on a silicon substrate, Nano Lett. **11**, 385 (2010).

[32] A. Fu and P. Yang, Lower threshold for nanowire lasers, Nat. Mater. **14**, 557 (2015).

[33] J. Wallentin, N. Anttu, D. Asoli, M. Huffman, I. Åberg, M. H. Magnusson, G. Siefer, P. Fuss-Kailuweit, F. Dimroth, B. Witzigmann, H. Q. Xu, L. Samuelson, K. Deppert, and M. T. Borgström, InP nanowire array solar cells achieving 13.8% efficiency by exceeding the ray optics limit, Science **339**, 1057 (2013).

[34] P. Kivisaari, J. Oksanen, and J. Tulkki, Current injection to free-standing III-N nanowires by bipolar diffusion, Appl. Phys. Lett. **103**, 031103 (2013).

[35] P. Kivisaari, I. Kim, J. Oksanen, and S. Suihkonen, Elimination of lateral resistance and current crowding in large-area LEDs by composition grading and diffusion-driven charge transport, Adv. Electr. Mat. **3**, 1700103 (2017).

[36] A. Myllynen, T. Sadi, and J. Oksanen, Current spreading in back-contacted GaInP/GaAs light-emitting diode, IEEE T. Electr. Dev. **67**, 1027 (2020).

[37] L. Riuttanen, P. Kivisaari, O. Svensk, J. Oksanen, and S. Suihkonen, Diffusion injection in a buried multiquantum well light-emitting diode structure, IEEE T. Electr. Dev. **62**, 902 (2015).

[38] M.-L. Lee, Y.-H. Yeh, Z.-Y. Liu, K.-J. Chiang, and J.-K. Sheu, Planar GaN-based blue light-emitting diodes with surface p-n junction formed by selective-area Si-ion implantation, IEEE T. Electr. Dev. **64**, 4156 (2017).

[39] M.-L. Lee, S.-S. Wang, Y.-H. Yeh, P.-H. Liao, and J.-K. Sheu, Light-emitting diodes with surface gallium nitride $p-n$ homojunction structure formed by selective area regrowth, Sci. Rep. **9**, 3243 (2019).

[40] O. W. Purbo, D. T. Cassidy, and S. H. Chisholm, Numerical model for degenerate and heterostructure semiconductor devices, J. Appl. Phys. **66**, 5078 (1989).

[41] P. Kivisaari, T. Sadi, J. Li, P. Rinke, and J. Oksanen, On the Monte Carlo description of hot carrier effects and device characteristics of III-N LEDs, Adv. Electr. Mat. **3**, 1600494 (2017).

[42] C. G. Van de Walle, Band lineups and deformation potentials in the model-solid theory, Phys. Rev. B **39**, 1871 (1989).

[43] I. R. Vurgaftman and J. R. Meyer, Band parameters for III–V compound semiconductors and their alloys, J. Appl. Phys. **89**, 5815 (2001).

[44] S. Bhattacharya, I. Baydoun, M. Lin, and S. John, Towards 30% Power Conversion Efficiency in Thin-Silicon Photonic-Crystal Solar Cells, Phys. Rev. Appl. **11**, 014005 (2019).

[45] M. Kantner, U. Bandelow, T. Koprucki, J.-H. Schulze, A. Strittmatter, and H.-J. Wünsche, Efficient current injection into single quantum dots through oxide-confined $p-n$-diodes, IEEE T. Electr. Dev. **63**, 2036 (2016).

[46] F. Römer and B. Witzigmann, Acceptor impurity activation in III-nitride light emitting diodes, Appl. Phys. Lett. **106**, 021107 (2015).

[47] J. Piprek, Comparative efficiency analysis of GaN-based light-emitting diodes and laser diodes, Appl. Phys. Lett. **109**, 021104 (2016).

[48] L. Cerutti, J. B. Rodriguez, and E. Tournie, GaSb-based laser, monolithically grown on silicon substrate, emitting at 1.55 μm at room temperature, IEEE Photon. Technol. Lett. **22**, 553 (2010).

[49] I. Radevici, J. Tiira, T. Sadi, S. Ranta, A. Tukiainen, M. Guina, and J. Oksanen, Thermophotonic cooling in GaAs based light emitters, Appl. Phys. Lett. **114**, 051101 (2019).

[50] I. Radevici, T. Sadi, and J. Oksanen, Thermophotonic cooling with light-emitting diodes, Nat. Photon. **14**, 205 (2020).

[51] H. Savin, P. Repo, G. von Gastrow, P. Ortega, E. Calle, M. Garín, and R. Alcubilla, Black silicon solar cells with interdigitated back-contacts achieve 22.1% efficiency, Nat. Nanotechnol. **10**, 624 (2015).

[52] K. Yoshikawa, H. Kawasaki, W. Yoshida, T. Irie, K. Konishi, K. Nakano, T. Uto, D. Adachi, M. Kanematsu, H. Uzu, and K. Yamamoto, Silicon heterojunction solar cell with interdigitated back contacts for a photoconversion efficiency over 26%, Nat. Energy **2**, 17032 (2017).

[53] N. M. Andrade, K. T. Settaluri, S. Fortuna, S. Hooten, K. Han, E. Yablonovitch, V. Stojanovic, and M. C. Wu, in *IEEE Photonics Conference*, Reston, USA, 30 September–4 October (VA, USA, IEEE, 2018).

[54] M. Levinshtein, S. Rumyantsev, and M. Shur, *Handbook Series on Semiconductor Parameters: Volume 1:* Si*,* Ge*,* C *(Diamond), GaAs, GaP, GaSb, InAs, InP, InSb* (World Scientific, Singapore, 1996).